Three-dimensional transition in the wake of bluff elongated cylinders

By K. RYAN, M. C. THOMPSON and K. HOURIGAN

Fluids Laboratory for Aeronautical and Industrial Research (FLAIR), Department of Mechanical Engineering, Monash University, Melbourne, Victoria 3800, Australia

Despite little supporting evidence, there appears to be an implicit assumption that the wakes of two-dimensional bluff bodies undergo transition to three-dimensional flow and eventually turbulence, through the same sequence of transitions as observed for a circular cylinder wake. Previous studies of a square cylinder wake support this assumption. In this paper, the transition to three-dimensional wake flow is examined for an elongated cylinder with an aerodynamic leading edge and square trailing edge. The three-dimensional instability modes are determined as a function of aspect ratio (AR = length to width). Floquet analysis reveals that three distinct instabilities occur. These are referred to as Modes A, B′ and S′ through analogy with the modes for circular and square cylinders. For aspect ratios less than approximately 7.5, Mode A is the most unstable mode. For aspect ratios greater than this, the most unstable mode switches to Mode B′. This has the same spatio-temporal symmetry as Mode B for a circular cylinder, but a spanwise wavelength and near-wake features more in common with Mode S for a square cylinder. The dominant wavelength for this mode is approximately two cylinder thicknesses, much longer than for Mode B for a circular cylinder. It is found that the critical Reynolds number for the onset of the Mode A instability varies approximately with the square root of the aspect ratio. On the other hand, the critical Reynolds number for Mode B′ is almost independent of aspect ratio. For large aspect ratios, the separation in Reynolds number between the critical Reynolds numbers is substantial; for instance, for $AR = 17.5$, these values are approximately 450 and 700. In fact, for this aspect ratio, the third instability mode, Mode S′, is more unstable than Mode A. These results suggest that the transition scenario for elongated bluff bodies may be distinctly different to short bodies such as circular or square cylinders. At the very least, the dominant spanwise wavelength in the turbulent wake is likely to be much longer than that for a circular cylinder wake. In addition, the reversal of the ordering of occurrence of the two modes with the different spatial symmetries is likely to affect the development of spatio-temporal chaos as a precursor to fully turbulent flow.

In conjunction with prior work, the current results indicate that nearly all three-dimensional instabilities of the vortex street can be identified as one of only a handful of transition modes.

1. Introduction

The formation of vortex structures in the wake of two-dimensional bluff bodies has been the subject of intense study and debate for close to a century (e.g. von Kármán 1911; Roshko 1954; Berger & Wille 1972; Williamson 1996). Much of this work

has focused on the circular cylinder, owing in part to the geometric symmetry and simplicity, engineering practicality, and variation in results obtained over a wide range of investigations (Roshko 1954; Bloor 1964; Gerrard 1966; Gaster 1971; and many others). The establishment of a Hopf bifurcation instability, leading to the transition from a steady wake flow field to laminar two-dimensional (von Kármán) shedding has been well documented (Gerrard 1978; Perry, Chong & Lim 1982). For a circular cylinder, this bifurcation occurs at $Re_{c1} \simeq 46$–47 (Dusek, Fraunie & Le Gal 1994). Further transitions result in the formation of three-dimensional vortex structures in the wake and eventually, with increasing Reynolds number, lead to turbulence. For a circular cylinder, when the Reynolds number exceeds a critical value $Re_{c2} \simeq 190$, the wake undergoes transition from two- to three-dimensionality. As the Reynolds number is increased through the critical value, the wake first undergoes transition to the Mode A instability, and as the Reynolds number is further increased, a second transition to Mode B shedding occurs (Williamson 1988). Despite the intense focus on circular cylinders, comparatively little work has been undertaken regarding the three-dimensional wake flow transition process for bluff bodies with other cross-sections with the implicit belief that the cylinder transition scenario is relatively generic, in terms of flow transitions, the order of those transitions and the route to turbulent flow. The work described in this paper aims to test this hypothesis for elongated cylinders with streamlined leading and blunt trailing edges. Effectively, this geometry allows wake transitions to be studied as a function of boundary-layer properties prior to shear-layer separation into the wake.

As the Reynolds number is increased above the critical Reynolds number ($Re_{c2} \simeq 140$–194) there is a discontinuous drop in both the Strouhal number (St) and base pressure coefficient (C_{bp}). Associated with this drop is the observation that the primary Kármán vortices undergo sinusoidal spanwise perturbations with (for a circular cylinder) a spanwise wavelength of 3–4 cylinder diameters (Brede *et al.* 1994; Williamson 1996). Over several shedding cycles, the initial spanwise waviness grows until vortex loops are formed and stretched in the braid regions to form counter-rotating streamwise vortex pairs. These have the same spanwise wavelength as the initial sinusoidal perturbations. Over successive primary Kármán vortex half-cycles, streamwise vortex structures form at the same spanwise location as their predecessors; however, their vorticity is of opposite sign; that is, the mode exhibits out-of-phase symmetry. The structure described above has been termed Mode A shedding by Williamson (1988) in his experimental analysis of the wake of a circular cylinder. Similar wake patterns have been observed experimentally by Brede *et al.* (1994) and Hammache & Gharib (1989).

A large range for the critical Reynolds number ($Re_{c2} \simeq 140$–194) has been experimentally recorded for the Mode A transition. This is partly due to the hysteretic (or subcritical) nature of the transition (Henderson 1997), but mostly due to end effects caused by three-dimensional flows at the cylinder ends. However, by suppressing extrinsic three-dimensionalities, Miller & Williamson (1994) observed the critical Reynolds number for Mode A transition of $Re_{c2} = 194$.

As the Reynolds number is further increased to $Re \approx 230$–250, a new mode of instability is intermittently observed, called Mode B (Williamson 1988). As the Reynolds number is increased beyond $Re = 250$, both observations and energy spectra indicate that Mode B becomes the dominant mode and Mode A is suppressed. For a circular cylinder, Mode B has a spanwise wavelength of approximately 1 diameter, and is conjectured to scale on the vorticity thickness of the braid shear layer (Williamson 1996). The spanwise wavelength remains approximately constant

over a broad Reynolds-number range (Mansy, Yang & Williams 1994); the remnants of Mode B have been observed experimentally at Reynolds numbers up to 10 000. Mode B exhibits in-phase symmetry; that is, successive streamwise vortex structures from each side of the wake have the same sign.

Observations by Williamson (1988, 1996) have been verified experimentally, numerically and theoretically by a number of authors. Thompson, Hourigan & Sheridan (1994, 1996) conducted (DNS) computational studies of the three-dimensional flow around a circular cylinder. Their work verified the existence, and critical spanwise wavelength, of both Mode A and Mode B. Hammache & Gharib (1989), Brede *et al.* (1994), Zhang *et al.* (1995) and Henderson (1997) have also, through independent experiments and simulations, verified the nature of both Mode A and Mode B in the cylinder wake. Miller & Williamson (1994) give results for the spanwise wavelengths, mode topology and critical Reynolds numbers that correspond very well with the numerical Floquet stability analysis performed by Barkley & Henderson (1996). These authors showed linear instability of spanwise Floquet modes close to the experimental values for both Mode A and Mode B. They found critical Reynolds numbers of 188.6 for Mode A, and 259 for Mode B. While the latter prediction is considerably higher than the experimental value, the linear theory assumes a two-dimensional base flow, while in reality, the flow is already markedly three-dimensional after the flow has undergone the Mode A transition. Owing to the nature of Floquet stability analysis, only intrinsic linear instabilities may be deduced, and the experimentally observed drop in both St and C_{bp} requires direct numerical simulations of the saturated wake state. Henderson & Barkley (1996) observed that Mode A is a hysteretic or subcritical transition. Henderson (1997) has observed the drop in base pressure associated with the transition to Mode A shedding (in line with a hysteretic or subcritical transition); however, it appears that the prediction of the magnitude of the drop requires a very large spanwise computational domain size. Williamson (1996) has associated the reduction with the spontaneous formation of large-scale vortex dislocations, which occur experimentally at the same critical Reynolds number as for Mode A. These large-scale vortex dislocations appear to be due to a nonlinear instability and occur naturally once the Mode A instability has reached a nonlinear saturated state.

To date, very little work has been conducted on the flow field around bluff bodies with cross-sectional geometry other than that of a circular cylinder. Zhang *et al.* (1995) experimentally observed the existence of a Mode C instability in the wake of a circular cylinder when a tripwire was placed adjacent to the cylinder in a direction transverse to the fluid flow, thus breaking the symmetry. The Mode C instability was found to have a spanwise wavelength of 1.8 cylinder diameters (between the wavelength of the other modes), and was found to occur when the tripwire was located within 1 diameter of the cylinder. Their results indicate that the suppression of the flow field near the boundary layer results in a Mode C instability occurring in preference to Mode A and Mode B. Numerical calculations performed by Zhang *et al.* (1995) supported their experimental observations. Robichaux, Balachandar & Vanka (1999) performed a Floquet stability analysis on a cylinder of square cross-section. Their model predicted the existence of a third mode of instability, which they denoted Mode S. While many physical features of this instability mode corresponded to those found in the experimental and numerical work of Zhang *et al.* (1995), Robichaux *et al.* (1999) did not refer to this instability as Mode C, as a trip wire was not required to artificially break the planar symmetry and trigger the instability. Within the parameter space modelled ($150 < Re < 225$), Mode S was found to be critical, but only after the other two modes had already undergone transition, and hence may not be observed

experimentally. Robichaux *et al.* (1999) found this mode was a subharmonic, with the period double that of the base flow. Blackburn & Lopez (2003) have shown that it is not a true subharmonic, but rather has a complex Floquet multiplier, with real part negative and a small complex component; this combination of complex coefficients means that the mode almost appears to repeat every second cycle. However, it is not a true subharmonic (or period-doubled mode). Such modes can exist either as travelling waves or modulated standing waves.

A considerable amount of work has also been done on the transition to three-dimensionality in the wake of a very thin splitter plate. Two three-dimensional instability modes have been identified which do not destroy the underlying two-dimensional Kármán wake and are referred to as 'Mode 1' and 'Mode 2', respectively (Lasheras & Meiburg 1990). Modes 1 and 2 were found to differ only in their symmetry properties, in particular, the spatial properties of Mode 2 agree closely with that described for Mode A; however, Mode 1 was found to have markedly different spatial properties to Mode B. Meiburg & Lasheras (1988) and Lasheras & Meiburg (1990) have suggested that both Mode 1 and Mode 2 are due to a hyperbolic instability in the braid region of the two-dimensional Kármán vortex street. However, as demonstrated by Julien, Ortiz & Chomaz (2004), a hyperbolic instability does not account for the spatial properties of Mode 2. Instead, they suggest that a hyperbolic instability within the braid region is 'slaved' to an elliptic instability within the vortex core. This finding is in agreement with the findings of Thompson, Leweke & Williamson (2001*c*) who investigated the transition mechanism for Mode A in the wake of a circular cylinder.

Previous work has not adequately addressed whether the results obtained for the circular cylinder wake describe all important three-dimensional instability modes observed for nominally two-dimensional cylindrical bodies of different geometries, or if the wake transition scenario observed for a circular cylinder is effectively the generic scenario for other cylinders. Blackburn & Lopez (2003), following the work of Barkley *et al.* (2000), have used group theoretical concepts to show that systems with the same symmetries as cylinder wake flow can only undergo transitions with the base flow period corresponding to the two spatio-temporal symmetries of Modes A and B. Apart from these, Neimark–Sacker transitions (secondary Hopf bifurcations of the periodic base flow), which generally have a period which is not commensurate with the base flow period, are also possible (e.g. Mode S). However, the ordering of transitions with the control parameter(s) can change, as well as the underlying physical mechanism. In addition, it is possible that different physical mechanisms can lead to different modes with the same spatio-temporal symmetries.

In the two examples above, a slight change in the geometry or symmetry has introduced other transition modes or changed the order of appearance of the modes. In view of this, this study focuses on numerical simulation of the flow around an aerofoil leading-edge blunt trailing-edge cylinder, chosen because it is a relatively simple geometry which limits shedding to a single point for each half of the wake. In addition, the geometry is specified by a single parameter, the aspect ratio, and hence the wake behaviour can be investigated as this parameter varies. Effectively, the aspect ratio controls the boundary-layer characteristics at the point of separation of the fluid into the wake.

2. Objective and approach

The aim of this study is to quantify the characteristics of the three-dimensional instabilities in the wake of a nominally two-dimensional bluff cylinder. The basic
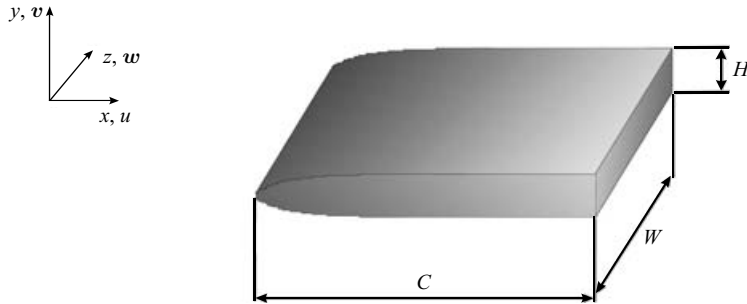
FIGURE 1. Generalized bluff-body geometry to be investigated showing important parameters.

set-up is shown in figure 1. The leading-edge geometry is chosen to be streamlined to prevent any vortex shedding into the boundary layer as it convects along the cylinder surface and into the wake. Experiments with a semi-circular leading edge showed that small boundary-layer vortices could occur at Reynolds numbers of order 1000 and possibly less (Welsh *et al.* 1990). An elliptical leading edge prevents this from occurring. For all numerical experiments described in this paper, the elliptic leading-edge has a major to minor axis ratio of 2.5:1. The cylinders have a square trailing edge such that vortices are shed at the same spatial location regardless of the Reynolds number. In each investigation, the cylinder is modelled as being immersed within a uniform homogeneous incompressible Newtonian fluid with constant inlet velocity U. The cylindrical geometry is described by a finite thickness (H), and finite chord or length (C) (again see figure 1).

There are two parameters governing the flow behaviour. The first is the aspect ratio, $AR = C/H$, and the second is the Reynolds number $Re = UH/\nu$, where ν is the kinematic viscosity. Within the scope of this investigation four aspect ratios were studied ($AR = 2.5, 7.5, 12.5, 17.5$), encompassing a non-equilibrium boundary layer at small aspect ratio to a near-universal boundary layer (prior to flow separation) for the larger aspect ratio studies. Through the course of the investigation, it was found that the critical Reynolds number range for three-dimensional transition increased substantially with aspect ratio. Hence, it was necessary to use higher Reynolds numbers for the larger aspect ratios.

Numerical modelling was performed in two stages. Initially, the time-dependent two-dimensional flow field around the cylinder is predicted by solving the time-dependent Navier–Stokes equations in two dimensions. Above the critical Reynolds number Re_{c1} two-dimensional instabilities saturate to form the familiar periodic flow field in the form of a Kármán vortex street of period T. The stability of this periodic two-dimensional base flow field to three-dimensional disturbances is then determined using Floquet stability analysis.

2.1. *Modelling the base flow*

The base flow field was obtained from the numerical solution of the two-dimensional time-dependent Navier–Stokes equations in primitive variable form

$$\frac{\partial \overline{\boldsymbol{u}}}{\partial t} + \overline{\boldsymbol{u}} \cdot \nabla \overline{\boldsymbol{u}} = -\nabla p + \nu \nabla^2 \overline{\boldsymbol{u}}. \tag{2.1}$$

Here, p is the kinematic pressure, ν is the kinematic viscosity and $\overline{\boldsymbol{u}} = (\overline{u}(t, x, y), \overline{v}(t, x, y))$ is the two-dimensional velocity vector. This vector equation is coupled with

the incompressibility constraint,

$$\nabla \cdot \overline{\boldsymbol{u}} = 0, \qquad (2.2)$$

to complete the set. These equations were solved using a high-order spectral-element method. The spatial accuracy is determined at run time by choosing the order of the tensor-product of interpolating polynomials within each macro-element as is usually possible with finite-element schemes. The method incorporates a three-step time-splitting method and achieves second-order time accuracy. Considerable testing and validation of the code has been undertaken and it has been applied successfully to related problems (Thompson *et al.* 1996, 2001*a*, *b*). Section 2.3 details the computational details specific to the current problem.

2.2. *Floquet stability analysis*

The base flow field's stability to three-dimensional disturbances was then determined as a function of Reynolds number and spanwise wavelength (λ). The same spectral-element code used to calculate the two-dimensional base flow field was extended to include the Floquet stability analysis technique.

The details of this are as follows. The velocity components and the kinematic pressure are expanded as the base fields plus a perturbation

$$u(t, x, y, z) = \overline{u}(t, x, y) + u'(t, x, y)\sin(2\pi z/\lambda), \qquad (2.3a)$$

$$v(t, x, y, z) = \overline{v}(t, x, y) + v'(t, x, y)\sin(2\pi z/\lambda), \qquad (2.3b)$$

$$w(t, x, y, z) = w'(t, x, y)\cos(2\pi z/\lambda), \qquad (2.3c)$$

$$p(t, x, y, z) = \overline{p}(t, x, y) + p'(t, x, y)\sin(2\pi z/\lambda). \qquad (2.3d)$$

The chosen sinusoidal z (spanwise) variation of the perturbation fields is appropriate to satisfy the linearized (and constant coefficient with respect to z) time-dependent three-dimensional Navier–Stokes equations for the perturbation fields exactly. Alternatively, complex forms for the z variation could be incorporated into the expansions. The choice of complex forms for the z variation allows the mode to be identified as a spanwise travelling mode or as a modulated standing wave; however, this is only of consequence if the Floquet multiplier is complex at transition. These cases can be detected using (2.3) since the real Floquet multiplier will be oscillatory. For cases in which this occurs, further analysis using the full complex form for the perturbation field was undertaken which allows modulated standing-wave and travelling-wave solutions to be obtained (see Blackburn & Lopez 2003, for example).

Using the full three-dimensional Navier–Stokes equations and linearizing gives the equations for the perturbation fields

$$\frac{\partial u'}{\partial t} + (\overline{\boldsymbol{u}} \cdot \nabla)u' + (\boldsymbol{u}' \cdot \nabla)\overline{u} = -\frac{\partial p'}{\partial x} + \nu\left(\nabla_{xy}^2 u' - \left(\frac{2\pi}{\lambda}\right)^2 u'\right), \qquad (2.4a)$$

$$\frac{\partial v'}{\partial t} + (\overline{\boldsymbol{u}} \cdot \nabla)v' + (\boldsymbol{u}' \cdot \nabla)\overline{v} = -\frac{\partial p'}{\partial y} + \nu\left(\nabla_{xy}^2 v' - \left(\frac{2\pi}{\lambda}\right)^2 v'\right), \qquad (2.4b)$$

$$\frac{\partial w'}{\partial t} + (\overline{\boldsymbol{u}} \cdot \nabla)w' = -\frac{\partial p'}{\partial z} + \nu\left(\nabla_{xy}^2 w' - \left(\frac{2\pi}{\lambda}\right)^2 w'\right), \qquad (2.4c)$$

$$\frac{\partial u'}{\partial x} + \frac{\partial v'}{\partial y} + \frac{\partial w'}{\partial z} = 0, \qquad (2.4d)$$

where $\nabla_{xy} = \tilde{\boldsymbol{\imath}}\, \partial/\partial x + \tilde{\boldsymbol{\jmath}}\, \partial/\partial y$.

According to Floquet theory, the velocity and pressure perturbations grow or decay exponentially from period to period. Thus, the perturbation fields satisfy the relationship

$$r'(t + T, x, y) = \exp(\sigma T)r'(t, x, y), \qquad (2.5)$$

where r' represents any of the perturbation fields (u', v', w' or p'). The coefficient $\mu = \exp(\sigma T)$ is often called the Floquet multiplier. If it is greater than unity, a perturbation at that wavelength will be exponentially amplified and hence result in three-dimensional flow. In reality, there are an infinite number of different modes with different Floquet multipliers, but the mode(s) of most interest are those corresponding to the largest Floquet multiplier, since it is that mode that grows fastest or decays slowest and hence will dominate. The Reynolds number corresponding to $\mu = 1$ is said to be the critical Reynolds number of inception (Re_{crit}). In experiments, this is the lowest Reynolds number above which the instability will be observed, provided the Reynolds number is increased from below. (The three-dimensionality may be maintained below this critical Reynolds number if the Reynolds number is decreased from above, provided the transition is hysteretic, as it is for Mode A.)

It is possible, using a suitable discretization, to use (2.4) and (2.5) to form an eigenvalue problem which can be solved to determine μ for any Re and λ. In practice, however, it is easier to integrate the perturbation equations forward in time directly, starting from a random perturbation field and renormalizing the fields at the end of each base flow period. After many cycles, only the dominant Floquet mode remains. At this point, the ratio of the mode amplitude to the amplitude exactly one period prior is equal to the Floquet multiplier for the dominant mode. (Here the amplitude is measured by the L_2 norm of any of the velocity perturbations.) The number of integration periods required depends on the ratio of the Floquet multipliers of the two most dominant modes. At the end of each period, the amplitude of the dominant Floquet mode relative to all others increases by at least this factor. Typically, in the simulations reported in this paper, 30–100 base flow periods were required to obtain results accurate to at least three significant figures.

In the computational code, the perturbation equations were discretized and integrated in time using the same spectral-element discretization used for the base flow. The base flow is simultaneously integrated forward in time, which is required to solve the perturbation equations. This procedure is slightly inefficient, since the base flow can be calculated independently and a Fourier time decomposition used to supply the base flow fields to the linearized perturbation equations (Barkley & Henderson 1996). However, it has the advantage of examining the pseudo-stability of non-periodic base flows. In addition, it has been implemented for a parallel computer cluster so that the base flow is calculated on one node and the Floquet modes corresponding to different wavelengths are simultaneously calculated on many other nodes; thus the inefficiency is reduced considerably.

2.3. *Computational details*

Four spectral-element meshes were used for the calculations, each corresponding to a different cylinder aspect ratio. The meshes were composed of N quadrilateral conforming macro-elements. Within each element, a tensor-product of Lagrangian polynomial interpolants of order n (in each direction) were used to approximate the solution variables. The front and side boundaries of the domain were set to a uniform background flow in the x-direction ($\bar{u} = U$). Zero normal velocity derivatives were used at the outlet boundary (while this can cause problems at higher Reynolds numbers, where it can prevent vortices from leaving the domain, it does not cause any degradation of
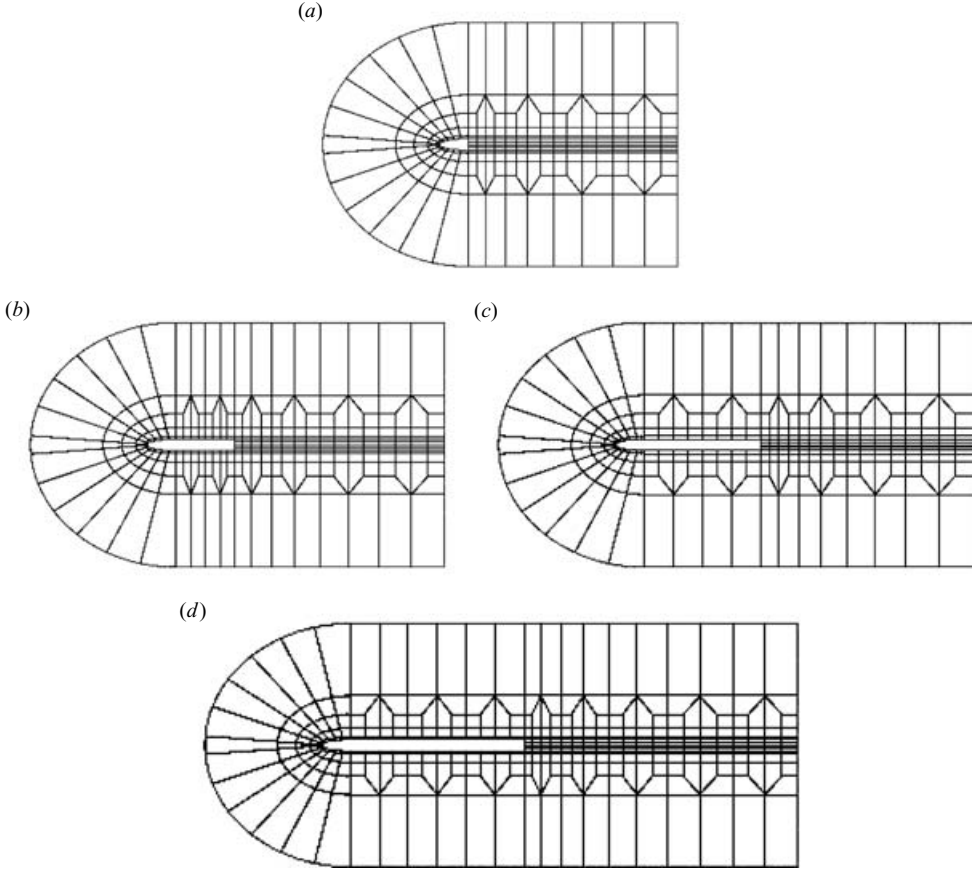
(*a*)

(*b*) (*c*)

(*d*)

FIGURE 2. Macro element meshes used for simulations, (*a*)–(*d*) correspond
to $AR = 2.5, 7.5, 12.5, 17.5$, respectively.

the solution accuracy in the neighbourhood of the cylinder for the Reynolds numbers
considered here). The boundary conditions for the perturbation velocity components
are: u', v', w' set to zero at the upstream and side boundaries; and zero normal
velocity gradient at the downstream boundary. The inlet length (l_i), taken as the
distance of the inlet to the leading edge, and the sidewall boundary width (l_w), taken
as the distance between the side boundary and the surface of the cylinder, were held
constant across all cylinder geometries. The outlet boundary length (l_o), taken as the
distance between the trailing edge of the cylinder and the outlet boundary, was varied
between the different geometries, such that cylinders with a larger aspect ratio were
modelled with more macro-elements. The meshes used for the investigation are shown
in figure 2. The geometrical parameters defining each mesh are given in table 1.

Mesh independence was established by performing a *p*-type resolution study. The
order of the Lagrangian polynomial interpolants within each element was successively
increased until the solution was mesh independent. A separate grid resolution study
was performed for each mesh. The Reynolds number employed in the grid resolution
study was the highest Reynolds number examined in further computations. The
Strouhal number, lift and drag coefficients were measured and compared across the
range of *n* investigated. The results for the aspect ratio $AR = 17.5$ grid at a Reynolds
number $Re = 700$ are summarized in table 2. For all measures employed, the variation

Dimension	$AR = 2.5$	7.5	12.5	17.5
$l_i/H, l_w/H$	10	10	10	10
l_o/H	18	18	18	23.5
N	321	321	321	401

TABLE 1. Mesh parameters for the different aspect ratios considered.

n	5	6	7	8	9	10	11	12
$C_{L(P)}$	2.8585	1.5516	1.7550	1.6231	1.6824	1.6684	1.6845	1.6874
$C_{D(P)}$	1.4252	0.9609	1.0598	0.9942	1.0231	1.0095	1.0159	1.0156
$C_{D(m)}$	1.4252	0.9609	1.0317	0.9661	0.9933	0.9806	0.9854	0.9853
St	0.2261	0.1752	0.1948	0.1840	0.1880	0.1861	0.1865	0.1865

TABLE 2. Convergence of global quantities with polynomial order n for the cylinder aspect ratio $AR = 17.5$ grid at $Re = 730$.

between the values at $n = 10$ and $n = 12$ is less than 1 %, which is representative of all the grids employed in this study. Ninth-order ($n = 10$) Lagrangian polynomial interpolants were used for the tensor-product expansion basis for all subsequent calculations.

A domain study was performed to evaluate blockage effects. As anticipated, the Strouhal number was found to be sensitive to the sidewall boundary width. Results from the p-type resolution study were crosschecked against a mesh with a larger inlet length $l_i = 22$, sidewall domain length $l_w = 22$, outlet length $l_o = 35$, and $N = 603$ elements. The study was only performed on the $AR = 17.5$ case, as this is the most sensitive to boundary location. The tests were performed at the highest Reynolds number examined in further computations for this mesh ($Re = 700$). The Strouhal number was found to vary by 3.5 % from the results from the grid for the smaller domain, and mean and peak drag forces were found to vary by 6 %. Despite this, the smaller domain sizes listed in table 1 were used in this study, principally for computational efficiency as it was felt that the physical mechanism governing the mode transition would not be affected by the smaller domain mesh size. In order to test this hypothesis, the Floquet multipliers over the full range of spanwise wavelengths, λ/H, reported in this study were calculated for the large mesh domain. The mode transition order and topology were found to be the same as that calculated for the smaller mesh domain size, as was the critical wavelength for each three-dimensional instability. The critical Reynolds number describing the transition from two- to three-dimensional flow was found to vary slightly with mesh domain size, with an accuracy of $\Delta Re = 3$.

In the following section, results from the Floquet stability analysis study are presented.

3. Results

3.1. *Two-dimensional results*

While not the main focus of this study, a summary of the base flow field results are presented in this section, in order to facilitate comparison of results with previous studies.
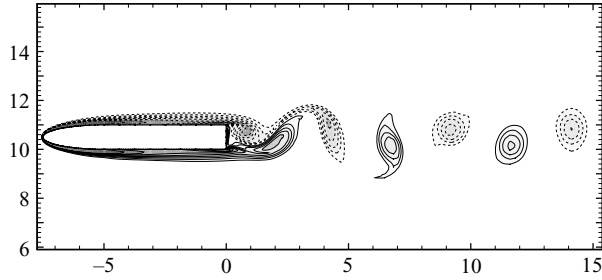
FIGURE 3. Spanwise vorticity field, ω_z, for $AR = 7.5$ and $Re = 400$. Contours are evenly spaced over the range $-4.0 \leqslant \omega_z \leqslant 4.0$; with $\Delta\omega_z = 0.5$. Vorticity has been non-dimensionalized by U_∞/H.
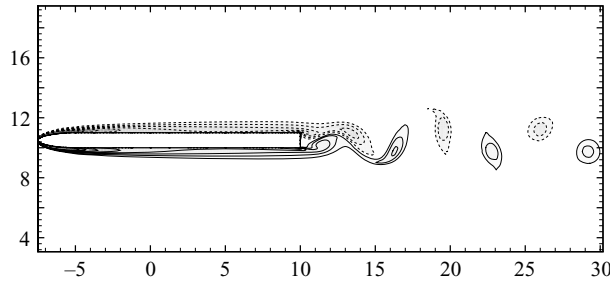

FIGURE 4. Spanwise vorticity field for $AR = 17.5$ and $Re = 400$. Contours are evenly spaced over the range $-4.0 \leqslant \omega_z \leqslant 4.0$; with $\Delta\omega_z = 0.5$.

Figure 3 shows typical equispaced contours of vorticity in the range $\omega_z = \pm 4$ for $AR = 7.5$. The Reynolds number for this case is $Re = 400$, based on the cylinder thickness. The vortex structures observed are consistent with those found for other cylinder aspect ratios investigated, as can be seen by comparing figure 3 with figure 4 which shows a snapshot of the vorticity field for the case of $AR = 17.5$, once again at $Re = 400$, based on the cylinder thickness. The vortex cores for the case of $AR = 7.5$ have a maximum vorticity of $\omega_z = \pm 2.5$. For the longer cylinder aspect ratio length case of $AR = 17.5$, the maximum vorticity measured in the positive forming vortex core is only $\omega_z = 1.5$.

The shedding frequency is presented in figure 5 in the form of the Roshko number (where $Ro = ReSt$), as a function of Reynolds number. Both the Reynolds number and the Roshko number use d' as the spatial scaling parameter, where d' is defined as $H + 2\delta$ and δ is the momentum thickness of the boundary layer measured at the trailing edge of the cylinder. By using d' as the spatial scaling parameter, the Roshko number results were found to form a linear relationship with Reynolds number. Our results are also directly comparable with the experimental results of Eisenlohr & Eckelmann (1989), who observed a linear relationship between Ro and Re independent of cylinder aspect ratio; their results are also presented in figure 5. The results for all aspect ratios simulated lie within the experimental scatter of Eisenlohr & Eckelmann's (1989) results.

Finally, the mean drag results are presented in figure 6 as a function of Reynolds number for the case of $AR = 7.5$, 12.5 and 17.5 (here the Reynolds number is based on the cylinder thickness only). For the case of $AR = 7.5$, the drag coefficient increases monotonically as a function of Reynolds number for $Re \geqslant 350$. For $AR = 12.5$, this
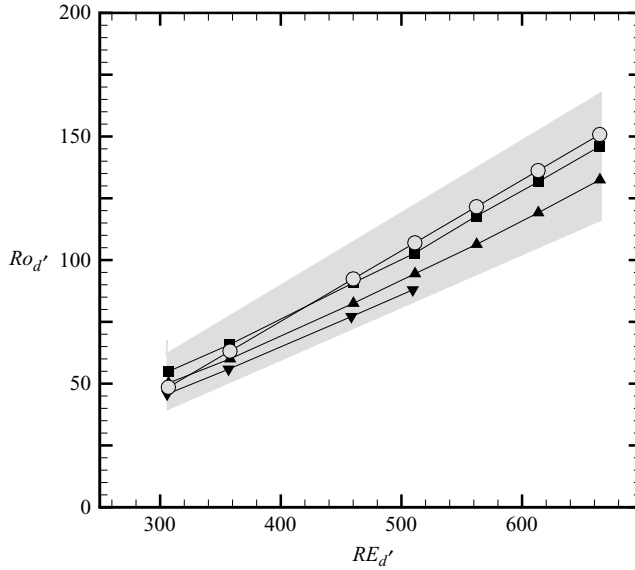
FIGURE 5. The shedding frequency, expressed as the Roshko number ($Ro = ReSt$), where for this figure both the Strouhal number and Reynolds number use d' as the length scale. —○—, experimental results of Eisenlohr & Eckelmann (1989); —■—, $AR = 7.5$ results; —▲—, $Ar = 12.5$ results; —▼—, $Ar = 17.5$ results. The shaded region is indicative of the spread in Eisenlohr & Eckelmann's experimental data.
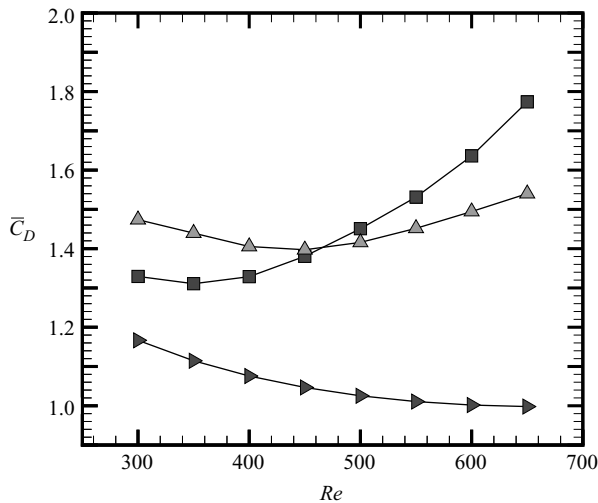

FIGURE 6. Time mean drag coefficient as a function of Reynolds number, for Reynolds numbers in the range $Re = [300, 650]$. —■—, $AR = 7.5$; —▲—, 12.5; —▶—, 17.5.

monotonic increase is less pronounced, and occurs only in the range $Re \geqslant 450$. For $AR = 17.5$, the drag monotonically decreases for all Reynolds numbers considered. A quantitative relationship between the mean drag results and the strength of the shedding vortices is presently being investigated.
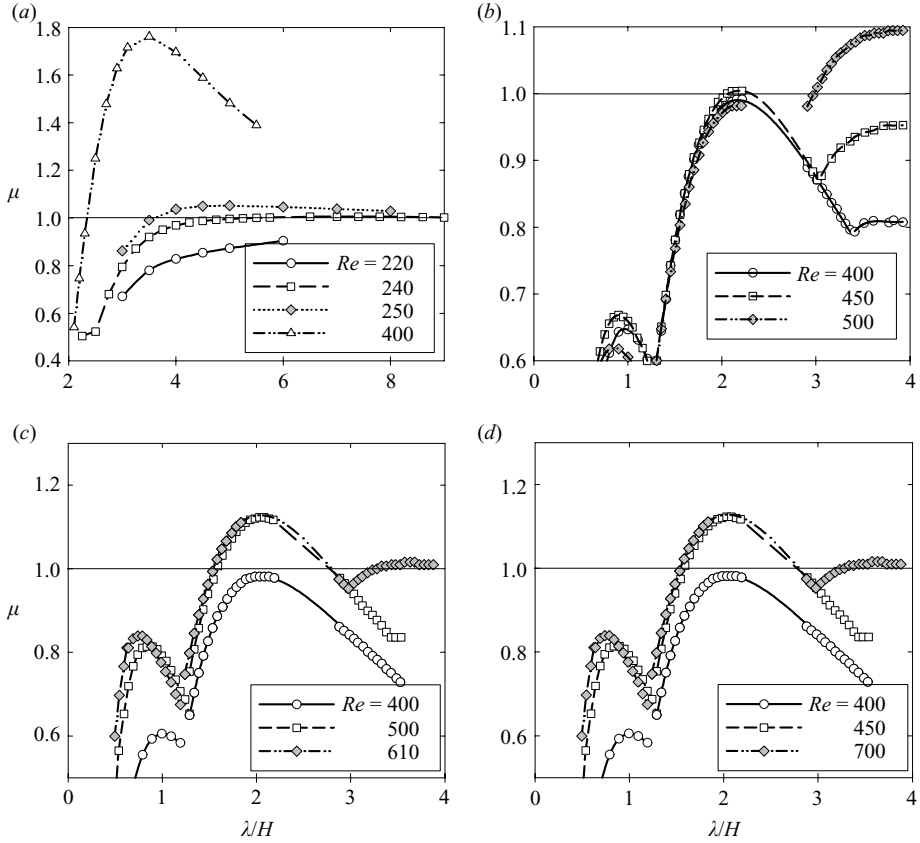
FIGURE 7. Floquet multipliers for the dominant modes at each spanwise wavelength for different Reynolds numbers. (*a*)–(*d*) correspond to $AR = 2.5$, 7.5, 12.5, 17.5 respectively.

3.2. *Floquet multipliers*

A Floquet analysis was performed for each aspect ratio over a range of Reynolds numbers. For each Reynolds number, a range of spanwise wavelengths was considered, including at least $0.5 < \lambda/H < 4.0$. Some simulations were performed for longer wavelengths to ensure that the dominant modes were captured. Once the critical Reynolds number for each mode was bracketed, interpolation was used to refine the estimate of the critical Reynolds numbers and corresponding wavelengths.

Figures 7(*a*)–(*d*) show the Floquet multipliers for the dominant modes for a range of spanwise wavelengths and Reynolds numbers. The figures refer to aspect ratios $AR = 2.5$, 7.5, 12.5 and 17.5, respectively.

Local maxima in these figures correspond to topologically different wake instability modes for the corresponding wavelength ranges. If the magnitude of the Floquet multiplier at a local peak exceeds unity, then the flow field is critically unstable to the mode at the particular wavelength. Again, this means that its amplitude will grow exponentially from background noise resulting in transition to three-dimensional flow.

3.2.1. *Aspect ratio 2.5*

Figure 7(*a*) shows Floquet multipliers for the $AR = 2.5$ case. For wavelengths in the range $0.5 \leqslant \lambda/H \leqslant 2.0$, no growing Floquet modes emerged from the iteration procedure within 100 cycles for $Re \leqslant 500$. For higher wavelengths, the procedure

(a)

(b)
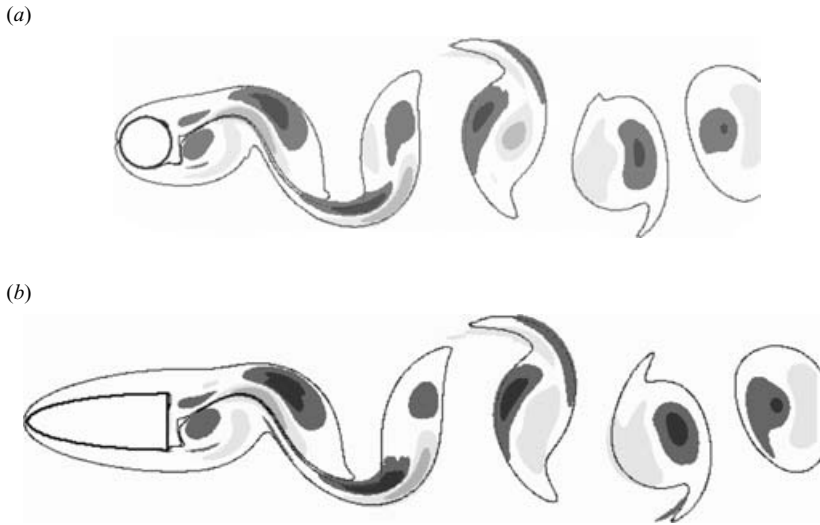

FIGURE 8. Comparison of the wake spanwise vorticity field of the Floquet mode for a circular cylinder ($Re = 190, \lambda = 4D$) and short aspect ratio cylinder ($AR = 2.5, Re = 240, \lambda = 4H$) showing the longer wavelength instability for the short aspect ratio cylinder is analogous to the Mode A instability of the circular cylinder. The spatial structure of the perturbation field relative to the position of the Kármán vortices is highlighted by the contours of spanwise vorticity with $\omega_z = \pm 0.2$. Both images are at approximately the same phase in the shedding cycle.

converged quickly (typically within 30 cycles for four significant figure accuracy) and the Floquet multiplier variation corresponding to the dominant mode is shown on the figure for different Reynolds numbers. The instability mode first becomes unstable for $\lambda/H \simeq 7$ at a Reynolds number of approximately 240. However, the instability is fairly broadband, and for $Re = 250$, the unstable range is $3.5 < \lambda/H < 10$. The upper limit is likely to be greater than this value, but no computations have been performed to confirm this. As the Reynolds number is increased, the most unstable wavelength is reduced so that for $Re = 400$ it is approximately $3.5H$.

The spatio-temporal symmetry and the perturbation field distribution for this mode are analogous to those of the Mode A instability for the circular cylinder (Williamson 1988). Figure 8 shows a comparison between coloured contours of spanwise perturbation vorticity for the Mode A circular cylinder wake at $Re = 190$ at $\lambda/H = 4$, and the $AR = 2.5$ cylinder wake for $Re = 400$ and $\lambda/H = 4$. The circular cylinder Floquet mode shown here has been calculated independently and agrees with the mode structure found by Barkley & Henderson (1996). Both wake instabilities show the same overall near- and far-wake structure and the same spanwise/streamwise vorticity topology, i.e. at the same spanwise location the spanwise/streamwise vorticity swaps sign between each Strouhal vortex pair.

3.2.2. *Aspect ratio 7.5*

Figure 7(b) depicts the Floquet multipliers for a cylinder of aspect ratio of $AR = 7.5$. Three distinct stability branches are observed for this case, corresponding to three topologically different instability modes. For the Reynolds number range investigated, the mode corresponding to the longest wavelength instability becomes critical at $Re \approx 470$ for $\lambda/H = 3.9$. Again, this mode is topologically similar to Mode A of the

(a)

(b)

FIGURE 9. Comparison of the wake streamwise vorticity field of the Floquet mode for the elliptical leading-edge cylinder ($AR = 7.5$, $Re = 450$, $\lambda = 2.2H$) and the circular cylinder ($Re = 259$, $\lambda = 0.8D$) showing the same spatial symmetries.

circular cylinder wake and the critical wavelength is similar. In addition, as for the circular cylinder, the instability quickly becomes relatively broadband as the Reynolds number is increased.

At $\lambda/H = 2.2$, another local maximum is observed. For $AR = 7.5$, this mode is approximately neutrally stable over the Reynolds number range simulated in this study ($400 \leqslant Re \leqslant 500$). Its spatio-temporal symmetry is analogous to that of the Mode B instability described by Williamson (1988). In figure 9, the spatial structure of the streamwise vorticity of the perturbation field is compared with that of Mode B for a circular cylinder wake ($Re = 259$ and $\lambda/H = 0.82$) at a similar point in the shedding cycle. The symmetry is such that the sign of streamwise vorticity is maintained from one half-cycle to the next. This is true of Mode B for a circular cylinder. However, there are some important differences in the perturbation field distributions. For the circular cylinder, the perturbation vorticity decays downstream much more quickly than for the cylinder geometry under investigation. This is not surprising given the lower critical Reynolds number and hence higher relative viscous diffusion. In addition, because the mode for the circular cylinder has a considerably shorter relative spanwise wavelength than that for the cylinder geometry considered here, the structures will be subject to more rapid diffusion anyway.

The difference in spanwise wavelength is surprising, especially given the wavelength predictions for the square cylinder (Robichaux *et al.* 1999) are similar to those for a circular cylinder if the length scale for the square cylinder is taken as the diagonal length. In both these cases, the ratio of the Mode B to Mode A wavelength is between 22 and 23 %. Here, this ratio is greater than 50 %. If fact, examination of figure 10, which shows the perturbation streamwise vorticity in the neighbourhood the newly forming vortices, reveals that the near-field spatial structure of the perturbation field has some important differences relative to the circular cylinder case. In the newly forming vortex in the top half of the vortex street, the perturbation field has swapped sign between the two different bodies. This is indicated by the circles overlaid on
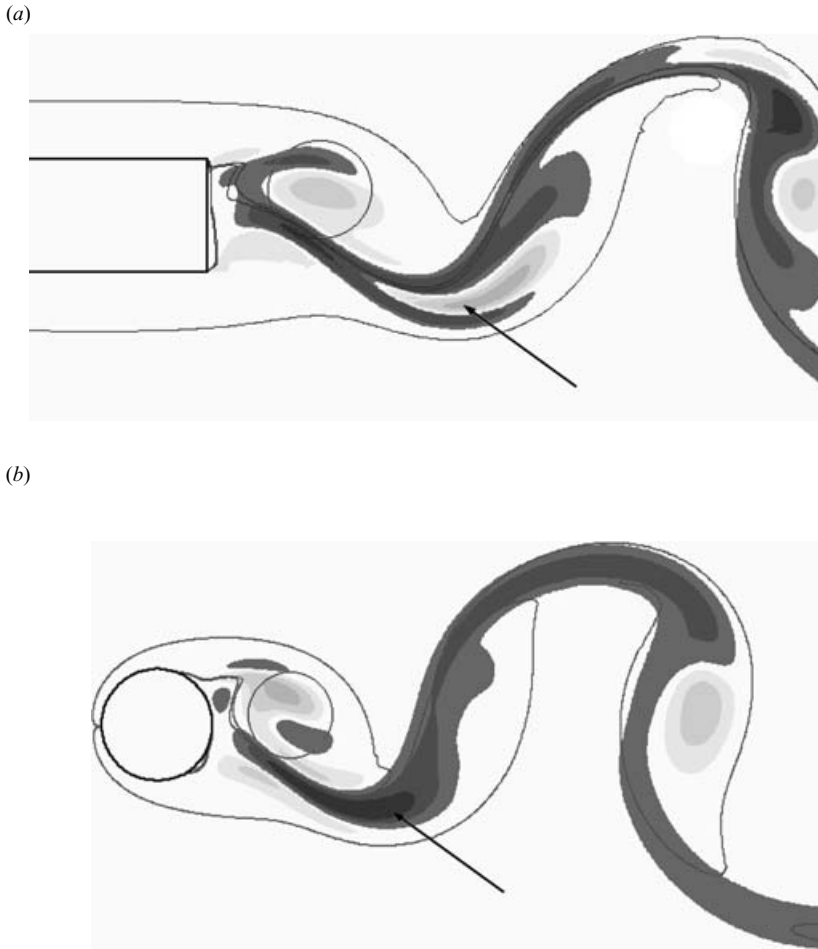
(*a*)

(*b*)

FIGURE 10. Enhanced view of streamwise vorticity field of the Floquet mode for the elliptical leading-edge cylinder ($AR = 7.5$, $Re = 450$, $\lambda = 2.2H$) and the circular cylinder ($Re = 259$, $\lambda = 0.8D$). The circles overlaid on the contour plots highlight the change to the spatial distribution of the vorticity in the newly forming vortices. The arrows show the effect on the downstream vorticity distribution half of a shedding cycle later.

the plots. One result of this reversal for the wake for the current cylinder geometry is that half a cycle later, the streamwise vorticity of opposite sign to the dominant streamwise vorticity pervading the braids is amplified, leading to a different local spatial structure at the corresponding downstream position. This is indicated by the arrows on the figure. Because of the differences in the near-wake perturbation field and the spanwise wavelength, we will refer to this mode as Mode B$'$.

At $\lambda/H = 0.9$–1.0, another local peak corresponding to a third instability mode is observed. This mode remains clearly subcritical up to the highest Reynolds number simulated for this cylinder aspect-ratio case. The value of λ/H corresponding to maximum growth varies with Reynolds number; a higher Reynolds number corresponds to a slightly smaller critical spanwise wavelength. The Floquet multipliers (μ) for this mode are oscillatory, indicating that the Floquet multiplier (corresponding to an analysis assuming complex eigenmodes) is actually complex. The Floquet analysis

FIGURE 11. Streamwise vorticity field of the Mode S′ instability ($AR = 7.5$, $Re = 500$, $\lambda = 1.0H$). The positions of the Kármán vortices are highlighted by the contours of spanwise vorticity of the base flow at $\omega = \pm 0.2$.

method described above cannot extract complex coefficients directly; however, the analysis was repeated assuming a complex perturbation field. Like the situation for the square cylinder (Robichaux *et al.* 1999), the mode has a complex Floquet multiplier close to minus one, and hence appears to be almost a subharmonic mode. However, as pointed out by Blackburn & Lopez (2003), a true subharmonic is extremely unlikely, and does not occur in this case either.

The wavelength of this mode is similar to that of Mode B for a circular cylinder wake, although the spatio-temporal symmetry is different. Figure 11 shows a snapshot of the streamwise perturbation field close to the end of the cylinder, similar to the snapshots revealing Modes B and B′ in figure 10. While the mode is time-varying from one shedding period to the next, this snapshot shows that the perturbation field structure in the newly forming vortex structure at the top of the trailing edge, and in the near-wake region, is perhaps more reminiscent of Mode B than is the intermediate wavelength Mode B′ instability discussed above. Thus, perhaps this instability has more in common with Mode B than Mode S (Robichaux *et al.* 1999) or Mode C (Zhang *et al.* 1995), even though Ryan (2004) has shown that the spatio-temporal symmetry is different. We will refer to this mode as Mode S′ (even though the mode is not a subharmonic) to relate it to the time-varying mode for a square cylinder (Robichaux *et al.* 1999).

3.2.3. *Aspect ratio 12.5*

As the cylinder aspect ratio is increased to 12.5 (figure 7*c*), Mode B′ is observed to become unstable at a lower Reynolds number than Mode A. Mode B′ is found to become critically unstable at a critical Reynolds number of $Re_{crit} \simeq 410$ for a critical wavelength of $\lambda/H \simeq 2.2$, whereas Mode A has a much higher critical Reynolds number of $Re_{crit} \approx 600$. This has experimental ramifications. It indicates that Mode B′ will be the first three-dimensional wake mode observed experimentally for long aspect-ratio elliptical leading-edge cylinders. For the circular cylinder wake, it appears that the rapid transition to a chaotic wake state is due to the nonlinear interaction of the A and B instability modes (Henderson 1997). Experimentally, Williamson (1996) has shown that Mode A, unlike Mode B, is not periodic in its saturated state even for a Reynolds number not far in excess of the critical value. Mode B has a relatively narrow instability wavelength band and is non-hysteretic, so for the geometry studied here, the swapping of the order of occurrence of two modes with different spatio-temporal symmetries may mean that the initial transition to three-dimensional flow is

much cleaner. Even at higher Reynolds numbers, the spectrum of wake wavelengths may be quite different to that found for a circular cylinder because of the order of transition and interactions between the modes, and the different apparent dominance of the intermediate wavelength mode which does not exist for the circular cylinder wake.

As for $AR = 12.5$, Mode S′ remains subcritical for the range of Reynolds numbers simulated. Once again, the amplification of the perturbation field has an oscillatory component indicative of a complex Floquet multiplier. The wavelength corresponding to the slowest decay rate was found to decrease slightly with increasing Reynolds number.

3.2.4. *Aspect ratio 17.5*

The results for this aspect ratio are similar to those for $AR = 12.5$. The Floquet multipliers are shown in figure 7(*d*). Once again, Mode B′ is found to become unstable first at a critical Reynolds number of $Re_{crit} \approx 430$. Mode A becomes unstable for $Re > 700$, with a preferred wavelength of approximately $3.5H$. Mode S′ was found to become critically unstable at $Re_{crit} \approx 690$ for $\lambda/H \approx 0.7$. Thus, both Mode B′ and S′ are more unstable than Mode A for this aspect ratio.

3.3. *Comparison of results for cylinders of different aspect ratios*

This choice of geometry allows a wider parameter space study than has been presented in previous work, focusing on the effect of alteration of bluff-body aspect ratio and, by implication, boundary-layer characteristics at separation, to the wake flow field. Previous studies (Roshko 1955) indicate that different bluff-body geometries generally have very similar primary wake structures. In this section, we speculate on the nature of the instabilities, the possible effect of the different orderings of critical Reynolds numbers for the onset of the instabilities, and the relationship to previous studies.

3.3.1. *Critical Reynolds numbers for transition*

Figure 12 depicts the critical Reynolds numbers for each three-dimensional mode transition as a function of cylinder aspect ratio. The curves represent approximate fits to the data. For Mode A, it was found that a relationship of the form $Re_{crit} \propto AR^{1/2}$ was found to fit the data well. For Mode B′, the transition Reynolds number remains approximately constant independent of aspect ratio. Note that for $AR = 7.5$, Mode B′ only reached approximately neutral stability ($\mu = 0.995$) at $Re = 440$. At higher Reynolds numbers, the maximum Floquet multiplier decreased slightly. Mode S′ becomes critical for $AR = 17.5$ but this is not shown on the figure.

3.3.2. *Mode A*

For all aspect ratios examined, Mode A is critically unstable at approximately the same spanwise wavelength of $3.5H$. This compares well with the experimentally observed wavelength of 3–4H (Williamson 1996) and the predicted critical wavelength of 3.96H (Barkley & Henderson 1996) for a circular cylinder wake. Also, as found for the circular cylinder, at Reynolds numbers not far in excess of critical, amplification of this mode occurs over a broad wavelength band. On the other hand, the critical Reynolds number increases significantly with aspect ratio: from $Re_{crit} \approx 240$ for $AR = 2.5$ to $Re_c \approx 700$ for $AR = 17.5$. The trend is shown in figure 12. As noted, a fit to the data points is shown, assuming a relationship of the form $Re_{crit} \propto (AR)^{1/2}$. While this is not perfect, it fits the data reasonably well.
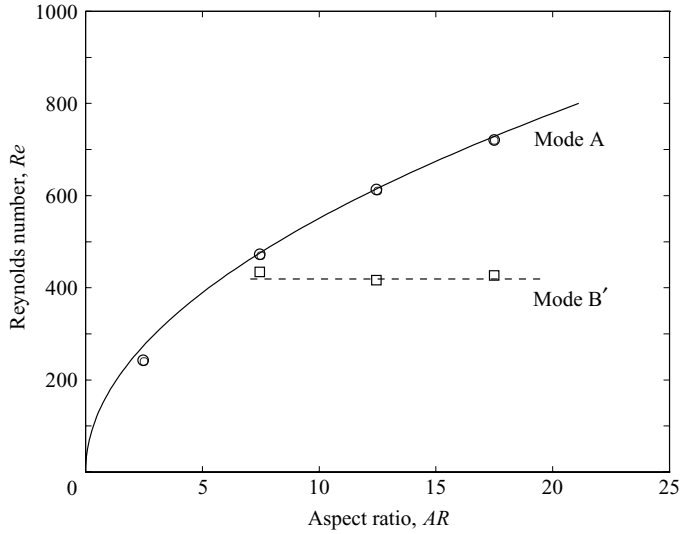
FIGURE 12. Critical Reynolds number for the different mode transitions as a function of cylinder aspect ratio. □, Mode B′ transition; ○, Mode A transition. The curves represent an approximate fit to the data.

While not directly apparent from figure 7, for each of the aspect ratios considered, Mode A was found to be connected to the neutral branch, in agreement with previous results for the circular cylinder.

It has been suggested (e.g. Williamson 1996; Leweke & Williamson 1998; Thompson *et al.* 2001*b*) that Mode A is predominantly an elliptical instability with the spanwise wavelength scaling on the length scale of the vortex cores. For a circular cylinder wake, the vortex perturbation pattern in the vortex cores appears to be clearly elliptical in nature in the wake downstream from the body. However, there has been considerable debate in the literature (e.g. Henderson 1997; Thompson *et al.* 2001*b*) on whether the elliptical instability mechanism is the cause in the instability in the near wake. The results for different aspect ratios are interesting in that the wavelength of the Mode A instability is approximately independent of aspect ratio and similar to that for a circular cylinder wake. For both circular cylinders and elliptical leading-edge cylinders, the length scale of the vortices is determined primarily by the body cross-section; the wake visualizations in this paper confirm this by showing that the vortex cores are similar in size for the different geometries. This is consistent with the hypothesis that the instability is an elliptic instability of the vortex cores.

According to standard laminar boundary-layer theory, the boundary-layer thickness (δ) can be approximated by

$$\delta = 5.0 \left(\frac{x}{Re} \right)^{1/2},$$

where x is the distance from the (virtual) origin and the Reynolds number is based on thickness H. Thus, for different aspect ratios, if the transition required that the boundary-layer thickness was similar as the flow enters the wake at the trailing edge, this should mean that the transition Reynolds number should vary in proportion to aspect ratio (x). This is clearly not the case, as indicated by the approximate fit described above. On the other hand, Landman & Saffman (1987) have suggested that

the growth rate (σ) of an elliptic instability is given by

$$\sigma = \sigma_{inviscid} - \Delta\sigma_{viscous}.$$

Here the inviscid growth rate is a function of the ellipticity of vortices; Eloy & Le Dizes (2001) have analysed the inviscid growth rate for a number of vortex profiles. Now suppose that the ellipticity of shed vortices is mainly dominated by convective effects rather than viscosity, once the vortices are shed. Assuming this, it follows that if the transition Reynolds number did vary in proportion to the aspect ratio, the boundary layer at the trailing edge would be similar, hence the ellipticity of the vortex structures in the wake should be similar and the first term contributing to the growth rate should be similar. The viscous correction is

$$\Delta\sigma_{viscous} \propto \frac{1}{Re(\lambda/H)^2},$$

where λ is the spanwise wavelength. This term reduces the amplification of short wavelength modes providing a short wavelength cutoff. An interpretation of Mode A in terms of elliptic instability theory is that the Reynolds number must be high enough so that the viscous correction term does not prevent the wavelength based on the core size from growing. We have seen that the inviscid contribution to the growth rate suggests the transition Reynolds number should be approximately proportional to aspect ratio. However, since the viscous correction to the growth rate is inversely proportional to the Reynolds number and the wavelength is primarily determined by core size (which is a proportional to thickness), the viscous correction to the growth rate should be less at higher Reynolds numbers hence the instability mode should already be growing. Hence, the theory suggests that the critical Reynolds-number dependence on aspect ratio should be less than linear. While this is not compelling evidence that an elliptical instability is the controlling generic instability mechanism for Mode A, it is at least consistent.

3.3.3. *Mode B′*

For aspect ratios between 7.5 and 17.5, a distinct instability mode with the same spatio-temporal symmetry as Mode B was found to become unstable. We have referred to this mode as Mode B′ based on its spatial symmetry. The critical wavelength was found to be approximately 2.2 cylinder thicknesses over the range of aspect ratios studied. The critical Reynolds number does not vary significantly with aspect ratio. Visualizations in the neighbourhood of the trailing-edge reveal that the perturbation field for Mode S′ has more in common with Mode B, than Mode B′. An interpretation may be that the spatio-temporal symmetry is perhaps not an ideal classification scheme. In this case, Mode S′ and Mode B also share a common relative spanwise wavelength, even though their spatio-temporal properties are different.

3.3.4. *Relative occurrence of Mode A, Mode B′ and Mode S′*

An increase in the aspect ratio alters the preferred mode of instability. For an aspect ratio of $AR = 7.5$, the initial instability is Mode A with a critical Reynolds number approximately equal to 475. As the aspect ratio is increased to 12.5, the critical Reynolds number for three-dimensional transition is approximately 450; however, Mode B′ is now the initial mode of instability, in preference to Mode A. As the aspect ratio is further increased to 17.5, the critical Reynolds number remains close to 450, and once again Mode B′ is the initial instability mode. As the aspect ratio is increased still further, the critical Reynolds number for the Mode A and

Mode B′ instabilities presumably becomes increasingly separated. Further increases in the aspect ratio may result in Mode A not becoming critical at all, or at least, the development and saturation of Mode B may lead to a distinctly different transition to turbulent flow which may not involve Mode A. For larger aspect ratios, even Mode S′ becomes unstable prior to Mode A, also suggesting a further possible alteration to the transition scenario.

3.3.5. *On the nature of modes*

A possible interpretation is that we can view these instability modes as a combination of idealized generic instability types such as elliptic, hyperbolic and centrifugal, with feedback from one cycle to the next to sustain the mode, but with possibly one mechanism governing the growth rate and wavelength selection. There is reasonable circumstantial evidence that this is the case for Mode A for a circular cylinder wake (e.g. Leweke & Williamson 1998; Thompson *et al.* 2001*b*) although dissenting views exist (Henderson 1998). Apart from the analysis above, other evidence comes from numerical simulations and experimental visualizations of Mode A which show invariant streamtubes as predicted by elliptic instability theory, and are consistent with the predicted spanwise wavelength and the growth rate in the core. Julien *et al.* (2004) have shown that the primary instability modes for an idealized Bickley wake also show strong elliptical character, in that the measured local growth rate is predicted well by elliptical instability theory, even though the perturbations migrate to, and are amplified in, the braid regions where the flow is hyperbolic. Conversely, the growth rates predicted by hyperbolic instability theory do not match the observed amplification rates. Julien *et al.* (2004) and others have suggested that the hyperbolic instability is *slaved* to elliptic instability which controls the growth rate and wavelength selection.

There is more doubt as to the nature of Mode B. Williamson (1996) and Leweke & Williamson (1998) suggest that the hyperbolic instability is the dominant mechanism, especially given that the mode appears to be located in the braids. Brede, Eckelmann & Rockwell (1996) have suggested that Mode B results from an instability of the separating shear layer in the near wake which they attribute to local centrifugal forces. In the case here, as noted, the mode is mostly concentrated initially between the forming vortices and in the braids between the vortices as the flow convects downstream. However, given the considerably longer spanwise wavelength than for the circular cylinder, the elliptical instability probably plays a stronger role in the cores and may support the maintenance of the instability.

3.3.6. *The possible role of centrifugal instability in the Mode B instability*

Although there has been speculation that a centrifugal instability may be the primary controlling mechanism involved in the development of the Mode B instability, as far as we are aware, little evidence has been published supporting this hypothesis. We explore this further in this section.

Figure 13 shows a plot of streamwise perturbation vorticity field at the time of maximum growth (see inset). The arrows show the position where the perturbation field is growing fastest. Streamlines have been generated using the velocity relative to the centre of the convecting newly forming vortex in the lower half of the wake. The streamlines are elliptical within the forming vortex structure. Outside this vortex, at the position where the perturbation growth is maximal, the streamlines converge to a hyperbolic point. In fact, the maximum growth occurs just inside this hyperbolic point towards the vortex centre. The instability growth measured by the rate of change of the maximum perturbation amplitude is approximately $7.2(U/D)^2$ at this time.
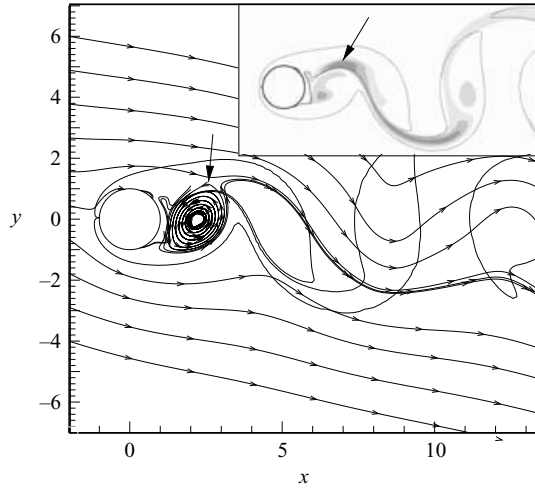
FIGURE 13. Streamlines for velocity field relative to the motion of the newly forming vortex centre. Spanwise vorticity contours ($\omega_z = \pm 0.2$) are overlaid to show the position of the wake vortices. The inset shows the streamwise vorticity field of the Mode B instability at the same time. The arrows show the position where the growth of the perturbation is a maximum.
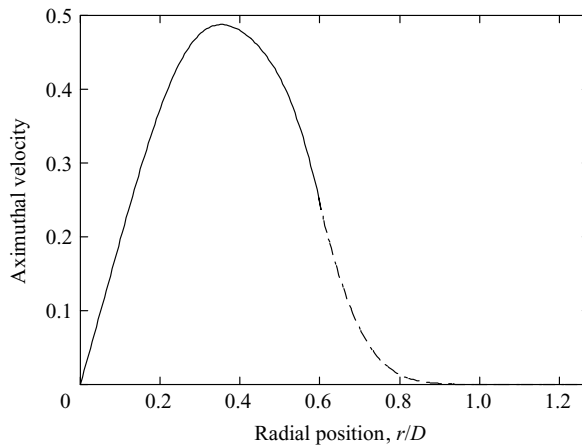

FIGURE 14. Azimuthal velocity field associated with forming vortex structure. The dashed line shows a Gaussian fit to reduce the velocity to zero smoothly.

As a test of the hypothesis that the centrifugal instability plays a dominant role in the growth of the instability and wavelength selection, the following procedure was carried out. The velocity field was extracted along a line from the vortex centre passing through the position where the perturbation growth was maximal. The velocity of the vortex centre was subtracted and this was used to construct an azimuthal velocity field for an isolated vortex, as shown in figure 14. The velocity field was only extended out to where the azimuthal velocity changes sign. This corresponds to approximately the position of the hyperbolic point shown in figure 13. A decaying Gaussian profile matching the function and the first derivative was used to reduce the velocity smoothly to zero. This is shown by the dashed part of the curve in the figure 14.
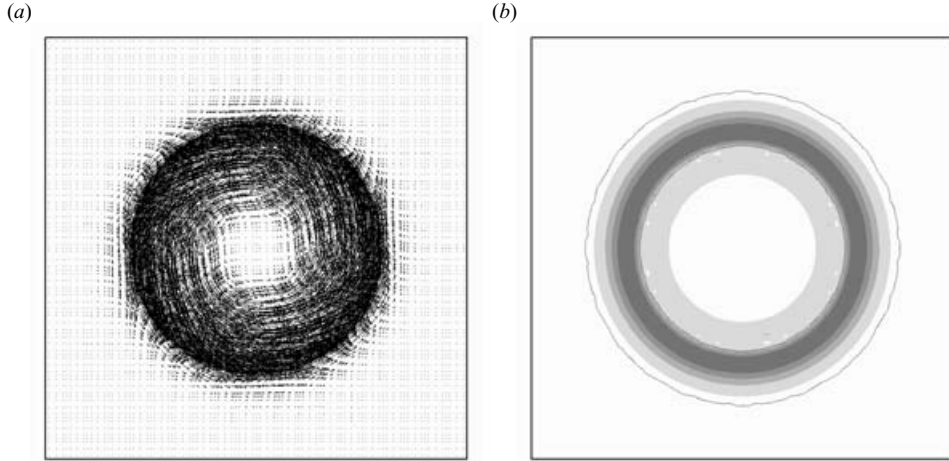
(*a*)   (*b*)

FIGURE 15. (*a*) Idealized azimuthal velocity field for the stability calculation. (*b*) Azimuthal vorticity of the centrifugal instability for $\lambda/D = 0.8D$ corresponding to the preferred wavelength of the Mode B instability from direct numerical simulations. The inner curve shows the position where the vorticity drops to zero and the outer curve indicates the approximate location of the hyperbolic point.
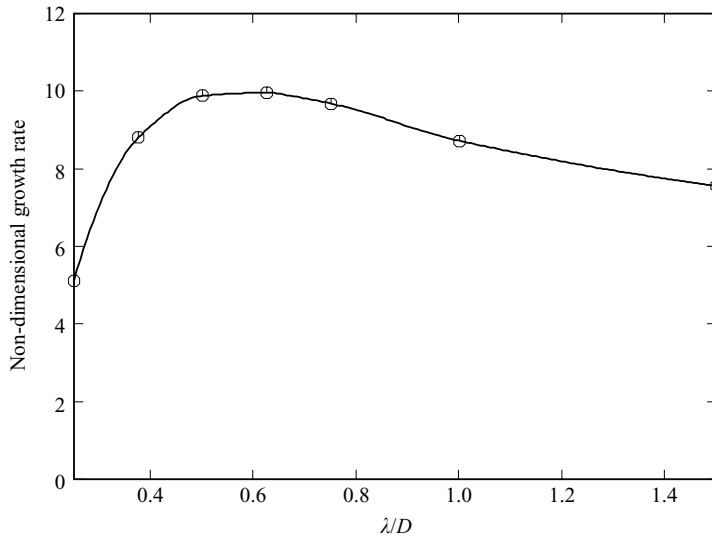

FIGURE 16. Predicted growth rate as a function of spanwise wavelength for the centrifugal instability model problem.

The linear stability of this velocity field, shown in figure 15(*a*), was then determined. To achieve this aim, this base flow field was frozen, and the linearized Navier–Stokes equations were solved to determine the growth rate as a function of spanwise wavelength. Figure 16 shows the predicted growth rate for the associated centrifugal instability. Figure 15(*b*) shows the perturbation azimuthal vorticity field corresponding to the maximum growth rate. The maximum growth rate was found to be about $10(U/D)^2$ corresponding to a preferred wavelength of about $0.6D$. These are not too far from the measured growth rate of 7.2 and the critical spanwise wavelength of 0.8,

especially given the latitude used in constructing the model. Importantly, figure 15(*b*) shows that the predicted maximum perturbation occurs at almost the precise location observed in the full numerical simulations.

Since the flow is evolving temporally, the favourable conditions for growth are probably only maintained for perhaps one quarter of a cycle. Given a Strouhal number of 0.2, this means that the total amplification is approximately $10(5/4) \approx 18$. The perturbation remains in the braids as it convects downstream, and the amplitude of the perturbation is maintained. This may be sufficient to produce an upstream influence from one half-cycle to the next half-cycle to maintain the instability.

Of course, this speculation applies to Mode B for a circular cylinder. Figure 10 shows that there are some distinct differences to the perturbation field between Modes B and B′, the latter showing a higher and more persistent perturbation amplitude in the core. As alluded to above, this may mean that the elliptical instability plays a stronger role for Mode B′, especially given the longer wavelength and therefore the reduced problem of the viscous cutoff. In addition, since the ellipticity of the core is maintained during the development of the wake, the elliptical instability is maintained for a long time, unlike the proposed centrifugal instability.

3.4. *Three-dimensional topology of the floquet modes*

The three modes found have been described in the previous sections for each aspect ratio investigated. In order to provide a similar base state, the three-dimensional structure of the wake flow field for each mode is presented for the specific case of cylinder aspect ratio $AR = 7.5$, and Reynolds number $Re = 400$. The Floquet mode topology for this case is representative of that found for other cylinder aspect ratio cases.

For each mode, the Floquet velocity field was computed and this was added as a small perturbation to the base flow to produce a flow field representative of the three-dimensional mode in the linear regime. As representative of Modes A, B′ and S′, perturbation fields were calculated for imposed spanwise wavelengths of $4H$, $2H$ and $1H$, respectively. For uniformity in the visualizations, the spanwise domain has been extended out to $12H$. This allows the spanwise variation to be observed and compared more easily.

Isosurfaces of positive and negative streamwise vorticity for Mode A are presented in figure 17. The spanwise vorticity is also plotted ($\omega_z = \pm 0.2U/D$) to highlight the position of the vortical structures instability field relative to the spanwise rollers in the wake. The swapping of the sign of streamwise vorticity from one half-cycle to the next is clearly apparent. As previously observed for Mode A, the perturbation field is strong in the braid regions between the rollers, although it is also strong inside the roller cores, but this is more difficult to discern from the plots.

Figure 18 shows similar isosurfaces for Mode B′. Twice as many spanwise structures are shown because of the reduced spanwise wavelength. At a given spanwise position, streamwise vorticity ω_x of a given sign is generated in a similar fashion to that found for a circular cylinder (Williamson 1996). The sign of ω_x, at a given spanwise location, remains constant over successive shedding cycles and forms a continuous chain of streamwise vorticity of the same sign. The similarity to the Mode B topological structure for a circular cylinder (Williamson 1996) is apparent, despite the much longer relative wavelength.

Figure 19 shows streamwise vorticity isosurfaces for Mode S′. This mode is distinctly different to Modes A and B′ as the spanwise wavelength is much smaller in comparison and the streamwise vorticity appears to swap sign approximately every full shedding

FIGURE 17. Isosurfaces of the streamwise vorticity field for the Floquet Mode A. Isosurfaces of spanwise vorticity ($\omega_z = \pm 0.2$) are also shown to indicate the positions of the Kármán vortices. ($Re = 400$, $AR = 7.5$).

period, which is why the corresponding mode for a square cylinder has been wrongly identified with a subharmonic mode previously. (Note that this Floquet mode structure was obtained from a complex Floquet mode calculation, which allows for travelling modes as well as spatially stationary modes (see Blackburn & Lopez 2003).

3.5. *Three-dimensional DNS calculations*

Floquet analysis has elucidated two important features of the Mode B′ instability in the wake of an aerodynamic leading-edge blunt trailing-edge flat cylinder. Mode B′ was found to have a consistent critical wavelength $\lambda/H = 2.2$ across all aspect ratio cylinders investigated; this value varies markedly from that for small-aspect bodies studied previously, i.e. either circular or square cylinders. Also, for sufficiently large cylinder aspect ratio, Mode B′ was found to precede the transition to Mode A; once again, in contrast to the observed ordering for circular and square cylinders. There was also evidence presented that the perturbation field in the near wake, and the spanwise wavelength, have more in common with Mode S of a square cylinder than Mode B. In order to verify these findings, and investigate the transition towards the saturated state, a three-dimensional direct numerical study was performed for an aspect ratio where Mode B′ is dominant and Mode A is also unstable. The Floquet analysis shows these criteria occur for $AR = 12.5$ and $Re = 600$.

Full three-dimensional simulations were undertaken using a Fourier/spectral-element code documented and validated in Thompson *et al.* (1996, 2001*a*), to explore the wake evolution from two-dimensional periodic flow to a fully three-dimensional
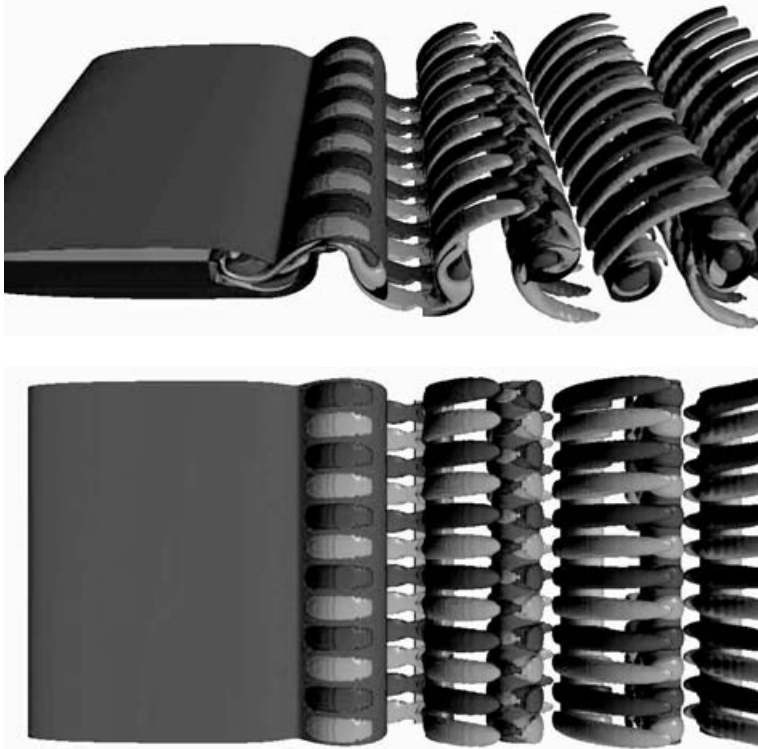
FIGURE 18. Isosurfaces of the streamwise vorticity field for the Floquet Mode B′. Isosurfaces of spanwise vorticity ($\omega_z = \pm 0.5$) are also shown to show the positions of the Kármán vortices. The selected spanwise wavelength is $2H$ with 6 wavelengths are shown. ($Re = 400$, $AR = 7.5$).

saturated wake flow. This calculation assumes a Fourier series representation in the spanwise direction and hence periodicity is enforced. This places a restriction on the allowable spanwise wavelengths, determining both the upper wavelength limit and the discrete wavelength spectrum. For the parameters discussed above, a spanwise domain size of $12H$ was chosen. This allows three Mode A wavelengths to fit inside the domain (and approximately 6 and 12 Mode B′ and S′ wavelengths). Sixty-four Fourier planes were used for the computation, corresponding to about 12 planes (6 modes) per Mode B′ wavelength. Whilst this is somewhat minimal, these full three-dimensional simulations are still computationally expensive. Experience indicates that this discretization should still provide reasonable resolution for the saturated mode.

Figure 20 shows streamwise and spanwise vorticity isosurfaces for the DNS investigation once the flow has reached a quasi-asymptotic state. The simulation was continued for approximately 30 shedding cycles after the wake saturated; however, at the end of this time, there was still some irregularity in downstream velocity traces at selected points. The simulation was discontinued at this time without resolving whether the final state would become truly periodic. The streamwise vortex structures shown here resemble the Mode B′ isosurfaces shown in figure 18. The main difference is the pinching together of the opposite signed vortex structures at their heads in line with many other studies (e.g. Henderson 1997). The spatial symmetry of the saturated mode is clearly identical to that of Mode B′. There are 6 wavelengths shown in the figure, indicating a selected spanwise wavelength of $2H$, consistent with the preferred

FIGURE 19. Isosurfaces of the streamwise vorticity field for the Floquet Mode C. Isosurfaces of spanwise vorticity ($\omega_z = \pm 0.5$) are also shown to show the positions of the Kármán vortices. Spanwise wavelength is $1H$ and 12 wavelengths are shown. ($Re = 400$, $AR = 7.5$).

wavelength of the Floquet mode. There is no visual evidence of any remnant of Mode A in the visualization, although perhaps this is not surprising given the relative amplification of Modes A and B′ at the Reynolds number of the simulation. At least, this simulation supports the findings of the Floquet analysis.

4. Conclusions

Floquet stability analysis has been presented quantifying the three-dimensional instability modes associated with the two-dimensional periodic base flow of an elliptical leading-edge square trailing-edge cylinder. The three modes show both some similarities to, and differences from, the three instability modes, A, B and S, previously identified for compact bodies. For very short bodies, Mode A is clearly dominant and it is expected that the transition scenario may be similar to that for a circular cylinder. For intermediate-aspect-ratio bodies ($AR > 7.5$), the intermediate wavelength instability mode, Mode B′, undergoes transition at the lowest Reynolds number. This mode has the same spatio-temporal symmetry of Mode B for a circular cylinder, but a much longer wavelength ($2.2H$ compared to $0.8D$), and there is evidence that these instabilities are distinctly different in the near field. For very long-aspect-ratio bodies, the difference in critical Reynolds numbers for Modes B′ and A becomes more substantial, indicating that Mode A may play a very much reduced role, if any, in

FIGURE 20. Streamwise vorticity contours from three-dimensional DNS calculation for $AR = 12.5$ and $Re = 600$ showing Mode B instability. ■ and ■ iso-surfaces represent ω_x, ■ iso-surfaces represent ω_z the cylinder is shown as ■.

the transition to turbulence. For $AR = 17.5$, the shortest wavelength instability mode is even more unstable than Mode A, again possibly affecting the transition scenario.

Sheard, Thompson & Hourigan (2003) investigated the three-dimensional instability modes for flow past a toroid with its axis parallel to the oncoming flow. As the aspect ratio is varied, this geometry bridges the gap between the axisymmetric geometry of a sphere (small aspect ratio) and that of a two-dimensional circular cylinder (infinite aspect ratio). There were different sets of instability modes depending on the aspect ratio. For large aspect ratios, three important instability modes were found: Modes A and B, analogues of the circular cylinder mode; and Mode C, the intermediate wavelength mode which is a subharmonic. In this case, it is possible for a true subharmonic to exist since the group properties of the system are different from those governing flow past a circular cylinder (Blackburn & Lopez 2003). Specifically, the symmetry about the cylinder centreplane no longer holds because of the curvature of the body. For intermediate aspect ratios, Mode C is the most unstable mode. Even though this is not strictly a two-dimensional cylindrical body, it is a related case and, like the situation for the bluff body considered in this paper, again indicates that transition may be less generic than previously assumed.

The possible role of the generic centrifugal instability in the generation and maintenance of the short wavelength Mode B instability of a circular cylinder wake was investigated. The model based on an isolated vortex with the same local properties where the instability growth rate was maximal, produced both a realistic growth rate

and spanwise wavelength. However, the conditions for growth are only maintained for part of a cycle. Hence, whether this limited growth is sufficient to maintain a feedback loop from one cycle to the next is a matter of debate. This situation differs somewhat from the speculation about Mode A being primarily due to an elliptic instability (e.g. Leweke & Williamson 1998; Thompson *et al.* 2001*b*; Julien *et al.* 2004), since the vortex cores are maintained during the propagation of the wake downstream and hence a lower but sustained growth may support the instability.

Finally, a full three-dimensional simulation was performed which produced a quasi-asymptotic state consistent with the findings of the Floquet analysis. Ideally, it would be advantageous to undertake simulations at significantly higher Reynolds numbers to investigate possible interactions between modes and transition to turbulence, but this would require very long integration times and be very expensive computationally. We are planning to investigate this problem experimentally in the near future.

REFERENCES

BARKLEY, D. & HENDERSON, R. 1996 Three-dimensional Floquet stability analysis of the wake of a circular cylinder. *J. Fluid Mech.* **322**, 215–241.

BARKLEY, D., TUCKERMAN, L. S. & GOLUBITSKY, M. 2000 Bifurcation theory for three-dimensional flow in the wake of a circular cylinder. *Phys. Rev.* E **61**, 5247–5252.

BERGER, E. & WILLE, R. 1972 Periodic flow phenomena. *Annu. Rev. Fluid Mech.* **4**, 313–340.

BLACKBURN, H. & LOPEZ, J. 2003 The onset of three-dimensional standing and modulated travelling waves in a periodically driven cavity flow. *J. Fluid Mech.* **497**, 289–317.

BLOOR, M. 1964 The transition to turbulence in the wake of a circular cylinder. *J. Fluid Mech.* **19**, 290–304.

BREDE, M., ECKELMANN, H., KÖNIG, M. & NOACK, B. R. 1994 Discrete shedding modes of the circular cylinder wake in a jet with a homogeneous core. *Phys. Fluids* **6**, 2711.

BREDE, M., ECKELMANN, H. & ROCKWELL, B. 1996 On secondary vortices in a cylinder wake. *Phys. Fluids* **8**, 2117–2124.

DUSEK, J., FRAUNIE, P. & LE GAL, P. 1994 Local analysis of the onset of instability in shear flows. *Phys. Fluids* **6**, 172.

EISENLOHR, H. & ECKELMANN, H. 1989 Vortex splitting and its consequences in the vortex street wake of cylinders at low Reynolds number. *Phys. Fluids* A **1**, 189–192.

ELOY, C. & LE DIZES, S. 2001 Stability of the Rankine vortex in a multipolar strain field. *Phys. Fluids* **8**, 660–676.

GASTER, M. 1971 Vortex shedding from circular cylinders at low Reynolds numbers. *J. Fluid Mech.* **46**, 749–756.

GERRARD, J. 1966 The mechanics of the formation region of vortices behind bluff bodies. *J. Fluid Mech.* **25**, 401–413.

GERRARD, J. 1978 The wakes of cylindrical bluff bodies at low Reynolds number. *Phil. Trans. R. Soc. Lond.* A **288**, 351–382.

HAMMACHE, M. & GHARIB, M. 1989 An experimental study of the parallel and oblique vortex shedding in the wake of circular cylinders. *Phys. Fluids* A **1**, 1611.

HENDERSON, R. 1997 Nonlinear dynamics and pattern formation in turbulent wake transition. *J. Fluid Mech.* **352**, 65–112.

HENDERSON, R. & BARKLEY, D. 1996 Secondary instability in the wake of a circular cylinder. *Phys. Fluids* **8**, 1683–1685.

HENDERSON, R. D. 1998 Turbulent wake transition. In *Proc. ASME Conf. on Bluff Body Wakes and Vortex-Induced Vibration, Washington DC*, article 31, pp. 1–7.

JULIEN, S., ORTIZ, S. & CHOMAZ, J.-M. 2004 Secondary instability mechanisms in the wake of a flat plate. *Eur. J. Mech.* B/*Fluids* **23**, 157–165.

KÁRMÁN, T. VON 1911 Flüssigkeits- u. Luftwiderstand. *Phys. Zeitschr. xiii* **49**.

LANDMAN, M. J. & SAFFMAN, P. G. 1987 The three-dimensional instability of strained vortices in a viscous fluid. *Phys. Fluids* **30**, 2339–2342.

LASHERAS, J. C. & MEIBURG, E. 1990 Three-dimensional vorticity modes in the wake of a flat plate. *Phys. Fluids* A **2**, 371–380.

LEWEKE, T. & WILLIAMSON, C. 1998 Three-dimensional instabilities in wake transition. *Eur. J. Mech.* B/*Fluids* **17**, 571–586.

MANSY, H., YANG, P. & WILLIAMS, D. 1994 Quantitative measurements of spanwise-periodic three-dimensional structures in the wake of a circular cylinder. *J. Fluid Mech.* **270**, 277–296.

MEIBURG, E. & LASHERAS, J. C. 1988 Experimental and numerical investigation of the three-dimensional transition in plane wakes. *J. Fluid Mech.* **190**, 1–37.

MILLER, G. & WILLIAMSON, C. 1994 Control of three-dimensional phase dynamics in a cylinder wake. *Exps Fluids* **18**, 26–35.

PERRY, A., CHONG, M. & LIM, T. 1982 The vortex shedding process behind two-dimensional bluff bodies. *J. Fluid Mech.* **116**, 77–90.

ROBICHAUX, J., BALACHANDAR, S. & VANKA, S. 1999 Three-dimensional floquet instability of the wake of square cylinder. *Phys. Fluids* **11**, 560.

ROSHKO, A. 1954 On the development of turbulent wakes from vortex streets. *NACA TR* 1191.

ROSHKO, A. 1955 On the wake and drag of bluff bodies. *J. Aeronaut. Sci.* **22**, 124–132.

RYAN, K. 2004 The analysis of wake structures behind stationary, freely oscillating and tethered cylinders. PhD thesis, Department of Mechanical Engineering, Monash University, Victoria, Australia.

SHEARD, G., THOMPSON, M. & HOURIGAN, K. 2003 From spheres to circular cylinders: stability and flow structures of bluff ring wakes. *J. Fluid Mech.* **492**, 147–180.

THOMPSON, M., HOURIGAN, K. & SHERIDAN, J. 1994 Three-dimensional instabilities in the cylinder wake. In *Intl Colloq. Jets, Wakes, Shear Layers*. Melbourne, Australia.

THOMPSON, M., HOURIGAN, K. & SHERIDAN, J. 1996 Three-dimensional instabilities in the wake of a circular cylinder. *Exp. Therm. Fluid Sci.* **12**, 190–196.

THOMPSON, M., LEWEKE, T. & WILLIAMSON, C. 2001*b* The physical mechanism of transition in bluff body wakes. *J. Fluids Struct.* **15**, 607–616.

THOMPSON, M. C., LEWEKE, T. & WILLIAMSON, C. H. K. 2001*c* The physical mechanism of transition in bluff body wakes. *J. Fluids Struct.* **15**, 607–616.

THOMPSON, M., LEWEKE, T. & PROVANSAL, M. 2001*a* Kinematics and dynamics of sphere wake transition. *J. Fluids Struct.* **15**, 575–585.

WELSH, M., HOURIGAN, K., WELCH, L., DOWNIE, R., THOMPSON, M. & STOKES, A. 1990 Acoustics and experimental methods: the influence of sound and heat transfer. *Expl. Thermal Fluid Sci.* **3**, 138–152.

WILLIAMSON, C. 1988 The existence of two stages in the transition to three-dimensionality of a cylinder wake. *Phys. Fluids* **31**, 3165–3168.

WILLIAMSON, C. 1996 Three-dimensional wake transition. *J. Fluid Mech.* **328**, 345–407.

ZHANG, H., FEY, U., NOACK, B. R., KÖNIG, M. & ECKELMANN, H. 1995 On the transition of the cylinder wake. *Phys. Fluids* **7**, 779–794.